Relationship between Three-dimensional Hydration Structures and Force Distributions Measured by Atomic Force Microscopy at Fluorite-Water Interfaces

Keisuke Miyazawa,[†] Naritaka Kobayashi,[†] Matthew Watkins,[‡] Alexander L. Shluger,[¶] Ken-ichi Amano,[§] and Takeshi Fukuma[*,†,∥]

Division of Electrical Engineering and Computer Science, Kanazawa University, Kakuma-machi, Kanazawa 920-1192, Japan, School of Mathematics and Physics, University of Lincoln, Brayford Pool, Lincoln LN6 7TS, United Kingdom, Department of Physics and Astronomy and London Centre for Nanotechnology, University College London, Gower Street, London, WC1E 6BT, United Kingdom, Department of Energy and Hydrocarbon Chemistry, Graduate School of Engineering, Kyoto University, Kyoto 615-8510, Japan., and ACT-C, Japan Science and Technology Agency, Honcho 4-1-9, Kawaguchi 332-0012, Japan

E-mail: fukuma@staff.kanazawa-u.ac.jp

Phone: +81 76 234 4847. Fax: +81 76 234 4632

---

[*]To whom correspondence should be addressed

[†]Division of Electrical Engineering and Computer Science, Kanazawa University

[‡]School of Mathematics and Physics, University of Lincoln, Brayford Pool, Lincoln LN6 7TS, United Kingdom

[¶]Department of Physics and Astronomy and London Centre for Nanotechnology, University College London

[§]Department of Energy and Hydrocarbon Chemistry, Graduate School of Engineering, Kyoto University

[∥]ACT-C, Japan Science and Technology Agency

Abstract

Hydration plays important roles in various solid-liquid interfacial phenomena. Very recently, three-dimensional scanning force microscopy (3D-SFM) has been proposed as the tool to visualise solvated surfaces and their hydration structures with lateral and vertical (sub)molecular resolution. However, the relationship between the 3D force map obtained and the equilibrium water density, $\rho(\boldsymbol{r})$, distribution above the surface remains an open question. Here, we investigate this relationship at an interface of an inorganic mineral, fluorite, and water. With improved experimental protocols in 3D-SFM, we obtained quantitative force maps in pure water in less than 20 minutes from submersion. This increase in the speed of measurement greatly expands the number of systems the method should be applicable to. The force maps measured in pure water are directly compared to force maps generated using the solvent tip approximation (STA) model and from explicit molecular dynamics simulations. The results show that the simulated STA force map reproduces the major features of the experimentally obtained force image. The agreement between the STA data and experiment establishes the correspondence between the water density used as an input to the STA model and the experimental hydration structure and thus provides a tool to bridge between the experimental force data and atomistic solvation structures. Further applications of this method should improve the accuracy and reliability of both interpretation of 3D-SFM force maps and atomistic simulations in wide range of solid-liquid interfacial phenomena.

Hydration plays an important role in various solid-liquid interfacial phenomena, including crystal growth,[1] electrochemical reactions[2] and biomolecular functions.[3–5] To understand the mechanism of these processes, non-uniform water density distributions, $\rho(\boldsymbol{r})$, (i.e. hydration structures) at solid-liquid interfaces have been intensively studied by spectroscopic methods using x-ray[6] or neutron[7] beam technologies, and mechanical methods such as surface force apparatus[8] and atomic force microscopy (AFM).[9] However, direct imaging of a hydration structure generally requires subnanometer-scale and three-dimensional (3D) spatial resolution, which has been difficult for conventional measurement techniques. A requirement that

these measurements should be relatively non-invasive, limits the application of approaches using charged particles (e.g. electron microscopies).

Recently, AFM techniques for imaging a 3D force distribution at a solid-liquid interface have been proposed.[10,11] In these methods, an AFM tip is scanned vertically as well as laterally in an interfacial space. During scanning, the variation of force applied to the tip, $F(\boldsymbol{r})$, is recorded to produce a 3D $F(\boldsymbol{r})$ image. However, realising the full potential of this powerful technique requires establishing the imaging mechanism and developing a practical algorithm to connect the force measurement to the underlying water density distribution about the interface, $\rho(\boldsymbol{r})$.

In this paper, for the first time, we make direct comparison of two theoretical models with experimental 3D force distribution measured using AFM in aqueous solution. This has been achieved by improvements in experimental technique and data processing, which now allow measurements to be made in pure water within 20 minutes of the sample being exposed to solution. This, in turn, allowed us to overcome the main difficulties in previous studies, which have been obtaining stable working conditions to take the measurements of dissolving surface and will thus greatly widen the number of systems accessible to this technique. Experimentally, it had been found to be significantly easier to work with (supersaturated) electrolyte solutions, which provide a larger signal and more stable system.[12] But, the electrolyte solution significantly complicates theory and simulation of the system, making detailed interpretations of images unreliable. Although the influence of a tip on the intrinsic hydration structure or the presence of ions in solution can affect the 3D force distribution, as we show below, the pure water measurements allow quantitative comparison of experimental data to forces predicted by two theoretical approaches. The resulting simple model provides a bridge between the experimental force data and atomistic solvation structures.

Atomistic simulations have been vital for our understanding and interpretation of atomic-scale AFM measurements in vacuum[13] and recently is solutions.[14] Harada and Tsukada investigated the correlation between free energy of the system and overlap between the tip

and sample hydration layers.[14] They found that an attractive $F(\boldsymbol{r})$ peak appears at a tip position where the tip and sample hydration peaks overlap with each other. Watkins and Shluger investigated the changes in potential energy and entropy during a tip approach to a $CaF_2(111)$ surface.[15,16] They clarified that potential energy increase caused by removal of water from the interface is largely compensated by the increase of entropy. Fukuma et al. performed detailed comparison between 3D $F(\boldsymbol{r})$ images obtained by experiments and simulation.[17] They showed that subnanometer-scale $F(\boldsymbol{r})$ contrasts mainly originate from the direct interaction between the tip apex atom and a hydration peak (i.e. localised enhanced $\rho(\boldsymbol{r})$ distribution) just under it. These simulations, however, use specific tip models and require high computational costs. They provided deep insight into the mechanisms of imaging in solutions, but are less practical for routine interpretation of the growing number of images and 3D force distributions at solid-liquid interface. There is a strong need for simpler, more general and efficient models.

Recently, a model describing the relationship between $F(\boldsymbol{r})$ and $\rho(\boldsymbol{r})$ distributions was proposed.[18,19] In the model, an AFM tip is approximated by a single water molecule (we refer to water, but the model is applicable to other solvents). Namely, $F(\boldsymbol{r})$ is approximated by the force that a water molecule would experience when it is held fixed at a specific site, $\boldsymbol{r}$. By a statistical-mechanical approach, the relationship between $F(\boldsymbol{r})$ and $\rho(\boldsymbol{r})$ is derived as[18,19]

$$F(\boldsymbol{r}) = \frac{k_B T}{\rho(\boldsymbol{r})} \frac{\partial \rho(\boldsymbol{r})}{\partial z},\qquad(1)$$

where k_B, T and z denote Boltzmann's constant, temperature and the vertical tip position with respect to the sample surface, respectively. Hereafter, we refer to this model as the solvent tip approximation (STA) model. If proven accurate, such a model can become a key ingredient in a practical method of deducing hydration structures from 3D AFM data: we can calculate an $F(\boldsymbol{r})$ image from a computed $\rho(\boldsymbol{r})$ and compare it with experimental

data, agreement implying the soundness of the calculated water density. However, due to the significant simplification made for deriving the STA model, its applicability should be carefully verified by both simulation and experiments.

In this study, we investigate the relationship between $F(\boldsymbol{r})$ and $\rho(\boldsymbol{r})$ distributions at a fluorite-water interface by experiments, explicit MD simulation of tip-substrate force and calculation based on the STA model and conclude that conversion of the $\rho(\boldsymbol{r})$ image to an $F(\boldsymbol{r})$ image by the STA model is the current best practice for image interpretation.

Results and discussion

3D distribution of $\rho(\boldsymbol{r})$, $F_{\mathrm{STA}}(\boldsymbol{r})$ and $F_{\mathrm{exp}}(\boldsymbol{r})$

The number of solid-liquid interfaces that have been studied by atomic-level AFM simulation is very limited.[14,15,17,20] Fluorite(111)-water interface is one of the few examples and hence suitable for detailed comparison between simulation and experiments. Fluorite (CaF_2) crystals are widely used for semiconductor lithography,[21] other laser technologies[22] and radioactivity investigations.[23,24] Their growth process in an aqueous environment is important not only for fabrication of industrial devices but also for understanding mechanism of biomineralisation, formation of tooth enamel,[25,26] desalination for oil recovery[27–29] and water purification.[30–32] Hydration structures formed at a fluorite-water interface strongly influences ion adsorption and desorption in these processes.

$CaF_2(111)$ surface rapidly dissolves in pure water to form islands made of calcium hydroxo complexes.[33,34] These interfacial processes prevent atomic-scale measurements after $\sim$20 min since the immersion of a fluorite substrate into water. To overcome this challenge, we developed measurement technique where 20 min is sufficient to obtain well resolved force maps and to perform the comparison to theory. This proves that it should be possible to examine the structure of a much wider variety of solvated mineral interfaces with atomic resolution in 3D.
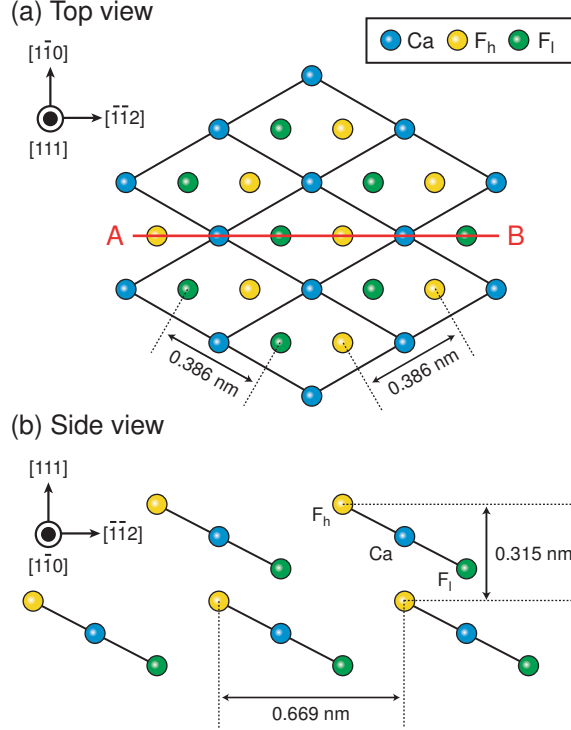
Figure 1: Crystal structure of fluorite(111) surface. (a) Top view. (b) Side view.

Fluorite (111) surface consists of hexagonally arranged Ca^{2+} and F^- ions as shown in Figure 1a. Among the F^- ions, some are higher and the others are lower than the Ca^{2+} ions. Here, we refer to the former as F_h and the latter as F_l as indicated in Figure 1b. All of the three ions (i.e. Ca, F_h and F_l) exist along Line AB in Figure 1a.

Figure 2 summarises the methods used in our work. In the experiment, we measured cantilever resonance frequency shfit $(\Delta f(\boldsymbol{r}))$ values while a tip was scanned in 3D at a fluorite(111)-water interface (Figure 2a). The obtained 3D $\Delta f(\boldsymbol{r})$ map was converted to a 3D force map using the Sader's equation.[35] By subtracting a long-range (LR) force component from it, we obtained a 3D short-range (SR) force map, $F_{exp}(\boldsymbol{r})$, (Figure 2b).

In the simulation, we calculate a $\rho(\boldsymbol{r})$ distribution at a fluorite(111)-water interface by MD simulation (Figures 2c and 2d).[15] The $\rho(\boldsymbol{r})$ distribution was converted to a force map using the STA model, $F_{STA}(\boldsymbol{r})$, (Figure 2e). The $F_{STA}(\boldsymbol{r})$ image is compared with the $F_{exp}(\boldsymbol{r})$ map.
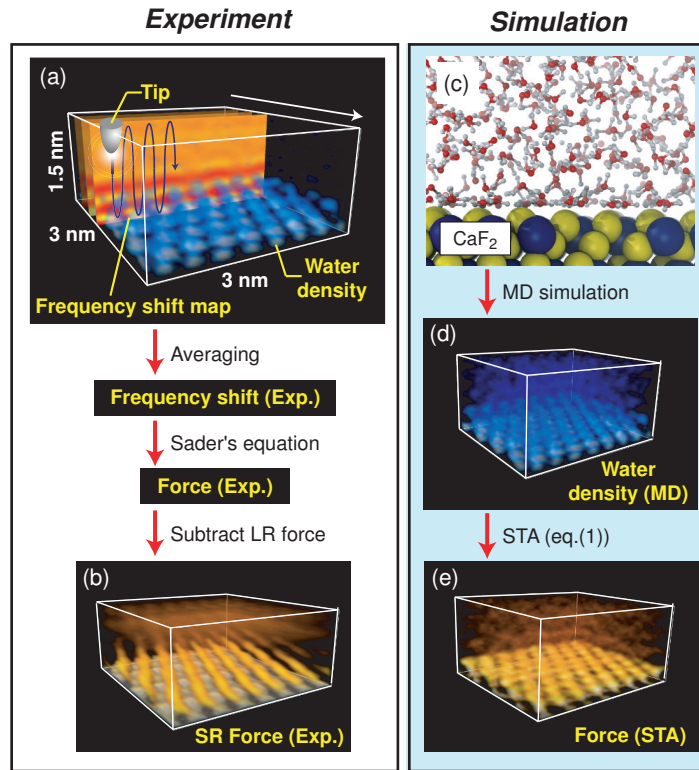
Figure 2: Outline of the methods used for obtaining 3D $F(\boldsymbol{r})$ maps at a fluorite(111)-water interface by experiment and simulation. (a) Measurement of 3D Δf distribution. (b) 3D SR $F(\boldsymbol{r})$ distribution converted from (a). (c) Snapshot of the MD simulation model. (d) 3D $\rho(\boldsymbol{r})$ distribution obtained by the MD simulation. (e) 3D $F(\boldsymbol{r})$ distribution calculated from (b) using the STA model.
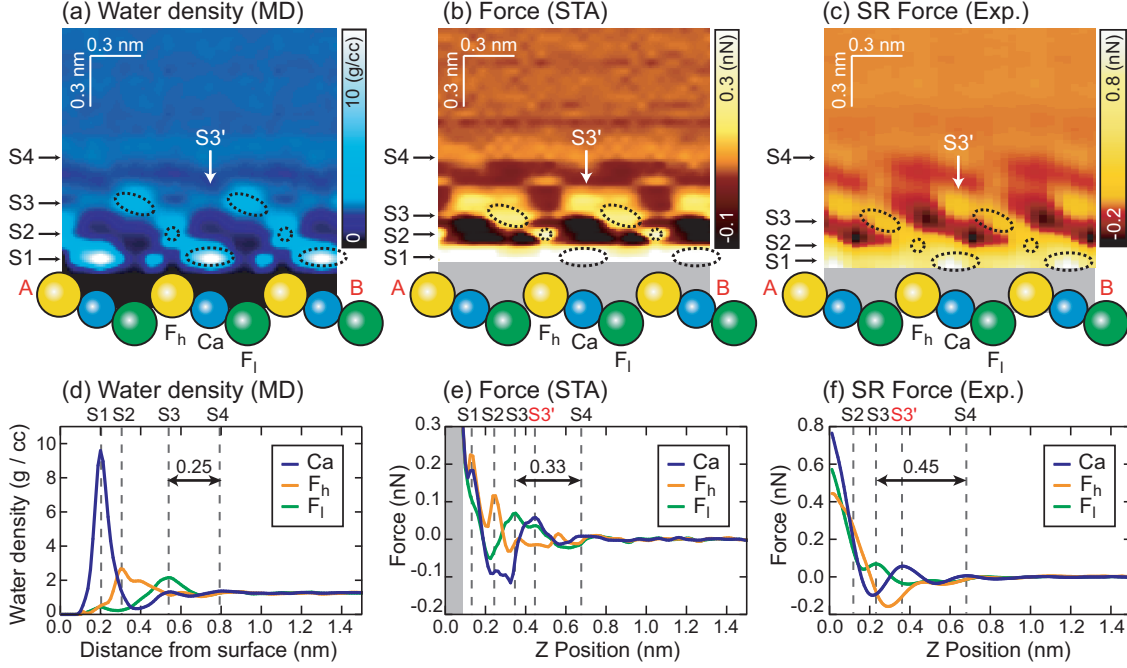
Figure 3: z cross sections of the (a) $\rho(\boldsymbol{r})$, (b) $F_{\text{STA}}(\boldsymbol{r})$ and (c) $F_{\text{exp}}(\boldsymbol{r})$ images. z profiles of the (d) $\rho(\boldsymbol{r})$, (e) $F_{\text{STA}}(\boldsymbol{r})$ and (f) $F_{\text{exp}}(\boldsymbol{r})$ images over Ca, F_h and F_l sites.

We extracted z cross sections along line A-B in Figure 1a through the $\rho(\boldsymbol{r})$ and $F(\boldsymbol{r})$ distributions (Figures 3a-c) to visualise their local distributions over the three special sites in one image. We plotted z profiles over each of the three sites for easier quantitative comparison (Figures 3d-f).

The z cross section of the $\rho(\boldsymbol{r})$ image (Figure 3a) shows localised enhanced contrasts (hydration peaks) above Ca, F_h and F_l sites as indicated by the circles with dotted lines. Here, we refer to each of the hydration peaks as S1, S2 and S3, respectively as we move away from the water-fluorite interface. Above these peaks, the image shows a layer-like enhanced contrast (hydration layer) which we will refer to as S4. The z profiles (Figure 3d) of the $\rho(\boldsymbol{r})$ image over Ca, F_h and F_l sites also show peaks corresponding to S1-S4. These profiles reveal that the peak corresponding to S1 is much larger than the others reflecting the strong attraction of water to the divalent cation.

8

Comparison between $\rho(\boldsymbol{r})$ and $F_{\mathrm{exp}}(\boldsymbol{r})$

We converted the $\rho(\boldsymbol{r})$ distribution to an $F_{\mathrm{STA}}(\boldsymbol{r})$ map using the STA model (i.e. Equation (1)). Figures 3b and 3e show z cross section and z profiles of the $F_{\mathrm{STA}}(\boldsymbol{r})$ image. Equation (1) shows that $F_{\mathrm{STA}}(\boldsymbol{r})$ is proportional to $(\partial\rho(\boldsymbol{r})/\partial z)/\rho(\boldsymbol{r})$. Thus, repulsive force peaks appear at locations where $\rho(\boldsymbol{r})$ is small but its gradient is large, namely, at a lower edge of a hydration peak. Consequently, the peak positions are shifted downwards by the $\rho(\boldsymbol{r})$ to $F_{\mathrm{STA}}(\boldsymbol{r})$ conversion process. To facilitate the comparison between the two images, the vertical position of the $F_{\mathrm{STA}}(\boldsymbol{r})$ is shifted upwards to match the S4 positions. Due to the contribution of the factor $(1/\rho(\boldsymbol{r}))$ in Equation (1), $F_{\mathrm{STA}}(\boldsymbol{r})$ goes to infinity near the sample surface where water is sterically forbidden from approaching. In Figures 3b and 3e, we indicated this z range with a grey background colour.

Qualitatively, similar features appear in both the $F_{\mathrm{STA}}(\boldsymbol{r})$ and $\rho(\boldsymbol{r})$ maps, such as the layer-like distribution of S4 and localised distributions of S1-S3 over Ca, F_{h} and F_{l} sites (circles with dotted lines). The similarity of the $F_{\mathrm{STA}}(\boldsymbol{r})$ and $\rho(\boldsymbol{r})$ maps can be understood by the observation that moving away from the surface, the $\rho(\boldsymbol{r})$ map over each site appears, to a reasonable approximation, as a damped sinusoidal function. The sinusoidal form means that the $(\partial\rho(\boldsymbol{r})/\partial z)$ factor in Equation (1) preserves the general form of the $\rho(\boldsymbol{r})$ map, but with a quarter wavelength shift - or approximately the radius of a water molecule. This result shows clearly why attempts to associate force peaks and troughs directly to water density has been broadly successful,[10,11] due to the qualitative similarity between $\rho(\boldsymbol{r})$ and $F_{\mathrm{STA}}(\boldsymbol{r})$ maps.

However, closer examination reveals significant differences between the two functions. The secondary hydration peak over the Ca site (S3′) is strongly enhanced in the $F_{\mathrm{STA}}(\boldsymbol{r})$ image as indicated by arrows in Figures 3a and 3b. Over the Ca site, the $\rho(\boldsymbol{r})$ value at the z position between S1 and S3′ ($z \simeq 0.4$ nm) is as small as 0.3 g/cc. Owing to the influence of the factor $1/\rho$ in Equation (1), this small $\rho(\boldsymbol{r})$ leads to an enhancement of the corresponding F_{STA} peak.

Another difference is that the vertical positions of S1-S3 in the $F_{\text{STA}}(\boldsymbol{r})$ image are shifted towards the surface compared to the $\rho(\boldsymbol{r})$ image, using the S4 position as a vertical reference. For example, the S3-S4 separation in the $\rho(\boldsymbol{r})$ profile is 0.25 nm, while it increases to 0.33 nm in the F_{STA} profile. In general, the individual peaks in the $\rho(\boldsymbol{r})$ profile have different shapes, and the magnitude of the peak shift caused by the conversion by Equation (1) is not constant. Therefore, peak separations in the $\rho(\boldsymbol{r})$ and $F_{\text{STA}}(\boldsymbol{r})$ maps are not necessarily the same.

This is an important finding. In previous studies, oscillatory force profiles were often attributed to a hydration force mainly due to the agreement between the size of a water molecule (0.25-0.30 nm) and the peak separations (0.2-0.4 nm).[9,36–38] However, the reported variation of the force peak separation is larger than expected from the size of a water molecule. So far, these discrepancies have tentatively been attributed to the influence of ions or the invasive nature of the tip during measurement.[39] In contrast, the above argument has clarified another mechanism to create such variations, even without any influence of ions in solution, with an *absolutely idealised tip model.*

Comparison between $F_{\text{STA}}(\boldsymbol{r})$ and $F\text{exp}(\boldsymbol{r})$

Similarly to the $\rho(\boldsymbol{r})$ and $F_{\text{STA}}(\boldsymbol{r})$ images, the $F_{\text{exp}}(\boldsymbol{r})$ image (Figure 3c) shows localised distributions corresponding to S1–S3 and a layer-like distribution corresponding to S4. In Figure 3c, the vertical position of the $F_{\text{exp}}(\boldsymbol{r})$ image is adjusted to match its S4 position to that of the $\rho(\boldsymbol{r})$ and $F_{\text{STA}}(\boldsymbol{r})$ images. In this case, the presence of the S4 layer may also provide a marker for calibrating the height of the tip above the surface.

The lateral alignment of the $F_{\text{exp}}(\boldsymbol{r})$ image is then adjusted to best match the 3D distribution in the $F_{\text{STA}}(\boldsymbol{r})$: This is perfectly reasonable to do as we do not know which image features correspond to which surface sites *a priori*. In the future it may be possible to devise numerical optimization schemes for the alignment - here we use symmetry to determine correct the correct slice to work with and a best judgement on the relative positions of the

various maxima and minima along the slice. If the agreement between theory and experiment is good this operation should be quite well defined. The arrangement of S1-S3 in the F_{exp} image is similar to that in the $\rho(\boldsymbol{r})$ and $F_{\mathrm{STA}}(\boldsymbol{r})$ images. Moreover, the other features of the $F_{\mathrm{STA}}(\boldsymbol{r})$ image, such as an enhancement of S3′ peak and downward shift of S1-S3 peaks, are confirmed in the $F_{\mathrm{exp}}(\boldsymbol{r})$ image. These features can be seen more clearly in the z profiles (Figure 3f). These profiles show that the S3-S4 separation in the $F_{\mathrm{exp}}(\boldsymbol{r})$ image (0.45 nm) is larger than that in the $\rho(\boldsymbol{r})$ image (0.25 nm). They also show that the magnitude of the S3, S3′ and S4 peaks in the $F_{\mathrm{exp}}(\boldsymbol{r})$ image approximately agrees with that in the $F_{\mathrm{STA}}(\boldsymbol{r})$ image.

This result indicates that $F_{\mathrm{STA}}(\boldsymbol{r})$ gives a much better overall description of $F_{\mathrm{exp}}(\boldsymbol{r})$ than $\rho(\boldsymbol{r})$, especially at larger distances from the surface. The overall shape of the force map is sufficiently detailed to allow a reliable assignment of the lateral alignment between theory and experiment - this means that we *identify the atomic sites at the surface*.
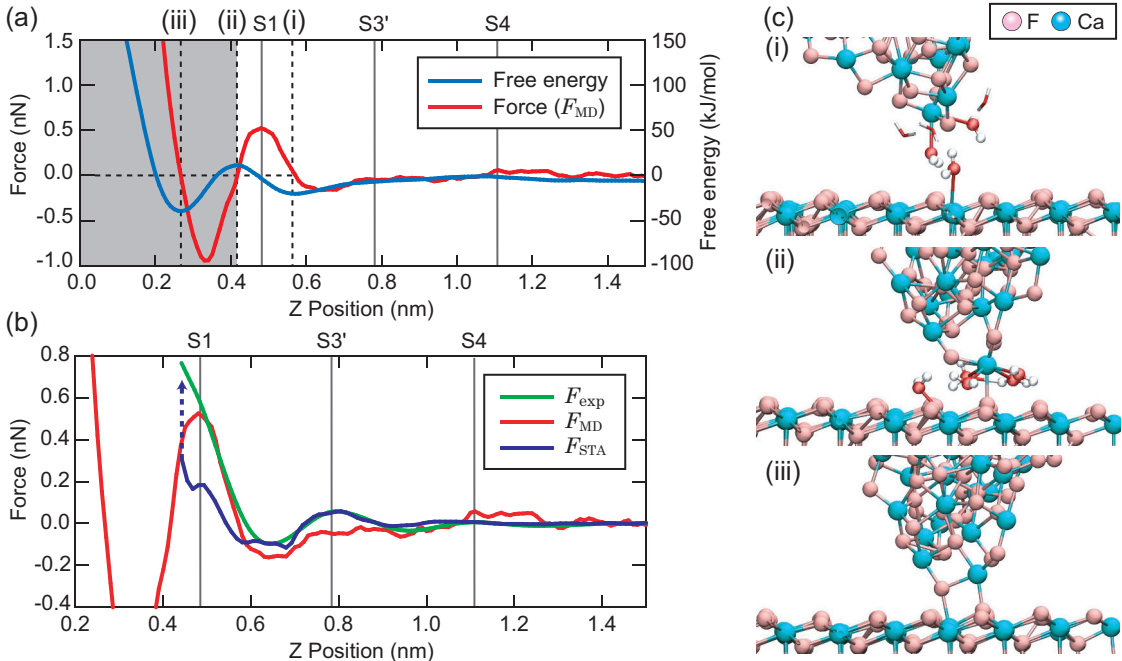

Figure 4: (a) Free energy and $F_{\mathrm{MD}}(\boldsymbol{r})$ profiles over a Ca site obtained by MD simulation. (b) $F_{\mathrm{MD}}(\boldsymbol{r})$, $F_{\mathrm{STA}}(\boldsymbol{r})$ and $F_{\mathrm{exp}}(\boldsymbol{r})$ profiles over a Ca site. (c) Snap shots of the MD simulation model for z tip positions (i)-(iii) indicated in (a).

11

Comparison between $F_{\mathrm{STA}}(\boldsymbol{r})$, $F_{\exp}(\boldsymbol{r})$ and $F_{\mathrm{MD}}(\boldsymbol{r})$

To make a connection to an atomistic picture of the measurement process, we briefly examine the results of atomic-scale MD simulation of the tip-surface interaction in water[15] and compare the results to the STA and experimental data. Previous comparison to simulations with explicit AFM tip models revealed modest agreement between the explicit modelling and the STA results.[18] Nevertheless, the 3D $F_{\mathrm{STA}}(\boldsymbol{r})$ and $F_{\exp}(\boldsymbol{r})$ show strong similarities, as seen in the last section, possibly suggesting that the AFM tip models used were not totally realistic, rather than a breakdown of the STA model.

Figure 4a shows the free energy and $F_{\mathrm{MD}}(\boldsymbol{r})$ changes during the approach of a CaF_2 cluster tip model over a Ca site. The $F_{\mathrm{MD}}(\boldsymbol{r})$ profile is obtained by differentiating the free energy profile with respect to z. Thus, the repulsive and attractive force peaks appear at the positions where the free energy profile shows the minimum and maximum slopes, respectively.

As the tip approaches the surface, the free energy gradually decreases to show a minimum at position (i). At this position, the first hydration peak just under the tip apex atom (T1) overlaps with S1 as indicated by the snapshot of the MD simulation in Figure 4c(i). At this tip-sample separation, there are energetically favorable interactions for water molecules with both tip and sample, leading to a reduction of the free energy.

With a further tip approach, the free energy increases to show a maximum at position (ii). During the tip approach process, water density continues to occupy the space between tip and sample. It is confined compared to the minima in the free energy at (i), leading to an increase of the free energy. When the tip reaches position (ii), the tip penetrates the confined water layer and starts to directly interact with the sample surface as indicated in Figure 4c(ii). This leads to a decrease of the free energy due to the release of the confined water as well as an attractive interaction between the tip and sample atoms.

At position (iii), the free energy has a minimum. At this position, the confined water layer is entirely removed and the multiple tip apex atoms directly interact with the surface atoms, as indicated in Figure 4c(iii). A further tip approach leads to a sharp increase of the

12

free energy due to the steric repulsion between the tip and sample atoms. These results show that the free energy change after the penetration of the last water layer strongly depends on the tip apex structure and properties.

Figure 4b shows the same $F_{\mathrm{MD}}(\boldsymbol{r})$ profile as shown in Figure 4a but with a magnified scale. To compare it with the $F_{\exp}(\boldsymbol{r})$ and $F_{\mathrm{STA}}(\boldsymbol{r})$ profiles, we also plotted them with their z positions adjusted to match the peak positions. As we cannot determine the absolute z tip position in an experiment, it is natural to adjust the z position of the $F_{\exp}$ profile with respect to the others. As for $F_{\mathrm{STA}}(\boldsymbol{r})$ and $F_{\mathrm{MD}}(\boldsymbol{r})$, their z positions are defined in the same way in the simulation box. Nevertheless, we needed to shift the z position of $F\mathrm{STA}(\boldsymbol{r})$ profile upwords by 0.35 nm to match the S4 position. The origin for this z position difference is later explained in Sec. .

Figure 4b shows that the $F_{\mathrm{MD}}(\boldsymbol{r})$, $F_{\mathrm{STA}}(\boldsymbol{r})$ and $F_{\exp}(\boldsymbol{r})$ profiles are similar in the z range above S1, i.e. at distances larger than a water molecule above the surface. In contrast, we find clear differences between them in the z range below S1. In this z range, $F_{\mathrm{MD}}(\boldsymbol{r})$ sharply decreases after the tip penetration of S1 and subsequently steeply increases. Thus, the $F_{\mathrm{MD}}(\boldsymbol{r})$ profile shows a clear repulsive peak corresponding to S1. In contrast, $F_{\exp}(\boldsymbol{r})$ and $F_{\mathrm{STA}}(\boldsymbol{r})$ continue to increase.

Physical reason for the agreement and disagreement between $F_{\mathrm{STA}}(\boldsymbol{r})$, $F_{\exp}(\boldsymbol{r})$ and $F_{\mathrm{MD}}(\boldsymbol{r})$

Above S1 position

In the STA model, a tip is approximated by a solvent molecule as shown in Figure 5a(i). A water molecule is attracted to the centre of a hydration peak. Thus, the water tip experiences an attractive or a repulsive force at an upper or a lower edge of a sample hydration peak, respectively (Figures 5a(ii) and 5a(iv)).

In a real experiment, we should consider the water tip as a hydration peak (T1) under
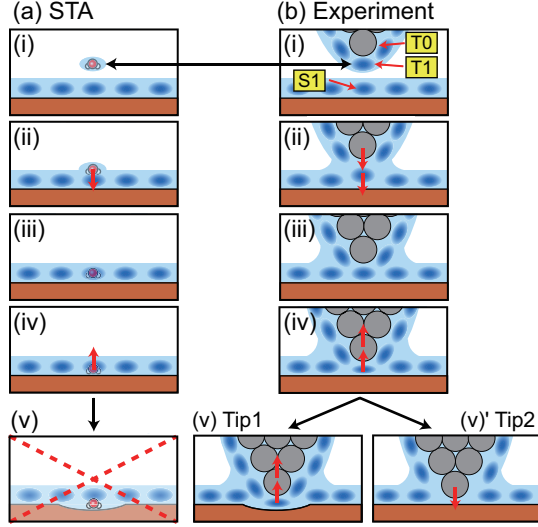
Figure 5: Schematic models showing relationship between a tip position and a measured force in (a) the STA model and (b) a real experiment.

the tip apex atom (T0) as shown in Figure 5b(i). An attractive or repulsive force applied to T1 is directly transmitted to T0. Therefore, F_{STA} can quantitatively agree with F_{exp}. This model explains the upward shift that we needed to apply to the $F_{STA}(\boldsymbol{r})$ profile in Figure 4b. In fact, the shifted distance (0.35 nm) approximately corresponds to the distance between T0 and T1.

Below S1 position

In the STA model, a water tip and a sample show no deformation (Figure 5a(v)). Thus, F_{STA} goes to infinity as soon as the tip contacts with the sample surface. This behavior is indicated by an arrow with a dotted line in Figure 4b. In a real experiment, a tip approach beyond S1 position leads to either of the following two events. For a rigid tip (Tip 1), force gradually increases due to confinement of S1 and deformation of a tip and a sample (Figure 5b(v)). This behavior corresponds to the $F_{exp}(\boldsymbol{r})$ profile in Figure 4b, which implies that the experimentally used tip has a relatively stable structure. For a flexible tip (Tip 2), force once decreases due to removal of T1 (Figure 5b(v)$'$), showing a clear peak corresponding to S1. This behavior corresponds to $F_{MD}(\boldsymbol{r})$ profile in Figure 4b. Thus, the tip used for the

14

MD simulation has a relatively high flexibility. In fact, the original tip structure at position (i) in Figure 4c is severely deformed when a repulsive force is applied to the tip just above position (ii) in Figure 4c.

As we see in Figure 4b, the $F_{\mathrm{STA}}(\boldsymbol{r})$ profile is closer to the $F_{\mathrm{exp}}(\boldsymbol{r})$ profile (rigid tip case) than the $F_{\mathrm{MD}}(\boldsymbol{r})$ profile. In our experiments, we hardly find a force profile showing a clear peak corresponding to S1. This result suggests that real tips used for an atomic-scale measurements mostly correspond to a rigid one. In an experiment, a cantilever mechanically oscillates at a frequency higher than 3.5 MHz. The repeated tip approach and retraction cycles may change an unstable tip structure into a stable one. In addition, at the beginning of an imaging experiment, we often see atomic-scale contrast changes but it settles down after several scans. During this process, the tip apex structure is probably stabilised.

Conclusions

We have investigated the relationship between 3D hydration structures and force distributions measured by AFM at a fluorite-water interface and performed a detailed comparison between 3D images of $F(\boldsymbol{r})$ measured by AFM, $\rho(\boldsymbol{r})$ calculated by MD simulation, and $F(\boldsymbol{r})$ calculated by the STA model. This comparison has been enabled by the improved experimental protocols allowing accurate force maps to be obtained in less than 20 minutes in pure water.

We propose that conversion of the $\rho(\boldsymbol{r})$ image to an $F(\boldsymbol{r})$ image by the STA model is the current best practice for image interpretation. The converted $F(\boldsymbol{r})$ image quantitatively reproduces the main features in the experimentally obtained $F(\boldsymbol{r})$ image in the z range above the first hydration layer on a sample (S1). However, we should consider that $F(\boldsymbol{r})$ calculated by the STA model represents $F(\boldsymbol{r})$ applied to the hydration peak just under a tip apex. In addition, the STA model cannot be used for calculating a force profile in the z range below S1 (i.e. $z < 0.25$ nm).

Good agreement between the STA model and experimental data implies very strongly that the underlying water density used as an input for the STA model is in good agreement with that probed experimentally by the AFM. The agreement between STA model and experiment also implies that the experimental measurement is essentially noninvasive at larger distances from the surface. The STA model only requires the calculation of the equilibrium solvent density above the interface, which will soon be tractable using *ab initio methods* for simple systems.

Figure 2 shows a practical scheme for the reconstruction of the solvent density by joint experiment and theory. It works by direct comparison of experimentally measured short range forces between the tip and hydration structures and the simulated force calculated from a simulated solvent density map using the STA model. Good agreement between the forces from experiment and theory increase the reliability of both. The underlying water density can be taken as a working model for the solvation structure at the interface where agreement between theory and experiment is good.

The proposed method should improve the accuracy and reliability of this measurement technique and lead to its future applications in various solid-liquid interfacial studies. The greatly improved speed of measurements makes the technique applicable to a large number of systems that would have been too unstable to measure previously.

Methods

Experimental.

Fluorite(111) surface rapidly dissolves in water to form islands made of calcium hydroxo complexes.[33] These interfacial processes prevent atomic-scale measurements after $\sim$20 min since the immersion of a fluorite substrate into water.[34] In practice, the optical alignment of a cantilever deflection sensor and tip coarse approach process take $\sim$10 min. Thus, 3D force images should be collected within $\sim$10 min, which is very severe experimental condition. To

overcome this difficulty, we used 3D scanning force microscopy (3D-SFM).[10] In the method, we modulate the z tip position with a sine wave while the tip is laterally scanned (Figure 2a). During the scan, $\Delta f(\boldsymbol{r})$ induced by the $F(\boldsymbol{r})$ variation is detected to form a 3D $\Delta f(\boldsymbol{r})$ image. Among several $\Delta f(\boldsymbol{r})$ measurement techniques proposed so far, 3D-SFM provides the highest imaging speed of less than 1 min/frame. This capability allows us to obtain a $\Delta f(\boldsymbol{r})$ image even in the very limited experimental time window available ($\sim$10 min).

Another problem is that force variation induced by a hydration structure in pure water is much smaller than that in electrolyte solution. In addition, the fast imaging requires a wide bandwidth in the force detection. This leads to a lower signal-to-noise ratio (SNR). Due to these severe experimental conditions, the SNR obtained by a conventional cantilever ($f_0 \simeq 150$ kHz) was insufficient for providing clear atomic-scale 3D force image. To solve this problem, we used an ultra-short cantilever (USC, Nanoworld) with a f_0 of 3.5 MHz in water.[40] This high f_0 greatly improves force sensitivity and hence enables atomic-resolution 3D $\Delta f(\boldsymbol{r})$ measurements even in pure water. To further improve the SNR, we applied an averaging filter using a pattern matching algorithm to the measured 3D Δf image (see Figure S1 in Supplementary Information for details). We converted the filtered 3D Δf image to a 3D $F_{\mathrm{exp}}(\boldsymbol{r})$ image using the Sader's equation.[35] From the 3D $F_{\mathrm{exp}}(\boldsymbol{r})$ image, we subtracted the long-range (LR) component (due to macroscopic effects) to obtain a 3D short-range (SR) $F_{\mathrm{exp}}(\boldsymbol{r})$ image (Figure 2b) (see Figure S2 in Supplementary Information for details). The obtained 3D SR $F_{\mathrm{exp}}(\boldsymbol{r})$ image shows clear atomic-scale contrasts, which should be directly comparable to forces calculated by the two computational methods as the data is (i) measured in pure water (ii) has long range macroscopic interactions subtracted out.

The AFM experiments were performed by a custom-built AFM with an ultra-low noise cantilever deflection sensor[41,42] and a high stability photothermal excitation system.[40,43] A commercially available phase-locked loop (PLL) circuit (OC4, SPECS) was used for oscillating a cantilever at its resonance frequency with constant amplitude and for detecting $\Delta f(\boldsymbol{r})$ induced by the $F(\boldsymbol{r})$ variation. The AFM head was controlled with a commercially available

AFM controller (ARC2, Asylum Research). We modified the control software to perform 3D force measurements. Size of the original 3D $\Delta f(\boldsymbol{r})$ image was $3 \times 3 \times 1.5$ mm^3 with $64 \times 64 \times 256$ pixels. The frequency and amplitude of the z modulation and the lateral scan speed during the 3D-SFM imaging were 195.3 Hz, 1.5 nm and 9.16 nm/s^{-1}, respectively. The whole 3D image was obtained in 53 s.

We used commercially available small cantilevers (USC-F5-k30, Nanoworld) with following modifications.[44] We removed an electron beam deposited (EBD) tip which comes with an as-purchased USC cantilever. Subsequently, we attached a silica bead with a diameter of 2 μm (43-00-203 Sicastar, Micromod) on the cantilever end. We fabricated an EBD tip with a length of approximately 500 nm and a tip apex radius of less than 10 nm using field emission scanning electron microscope (FE-SEM) (ERA-8000FE, ELIONIX) with a 30 kV accelerating voltage on the attached silica bead. Just before the AFM experiment, we coated the cantilever with Si (30 nm) using a dc sputter coater (K575XD, Emitech) to improve the reproducibility of the atomic-scale AFM imaging.[45] The f_0 and Q factor (Q) in liquid, and the spring constant (k) of the cantilever were 3.91 MHz, 9.6 and 106.0 N/m^{-1}, respectively.

We used fluorite(111) substrate with a size of $10 \times 10 \times 2$ mm^3 (Crystal Base). The substrate was glued onto a sample holder and cleaved with a razor blade. Immediately after the cleavage, we dropped 50 μL of water onto the substrate and performed AFM experiments at room temperature.

Theoretical.

Extensive details of the calculations used in this paper and discussions on the accuracy of various free energy methods, can be found in reference.[46]

The $\rho(\boldsymbol{r})$ distribution of water at a fluorite(111)-water interface was calculated by MD simulation, and is shown in Figures 2c and 2d.[15] From the obtained $\rho(\boldsymbol{r})$ distribution, a $F(\boldsymbol{r})$ map was obtained using the STA model, $F_{\text{STA}}(\boldsymbol{r})$, (Figure 2e).

Force versus distance curves over special sites of fluorite(111) surface were calculated

using MD simulation with an explicit AFM tip model, $F_{\mathrm{MD}}(\boldsymbol{r})$ (Figure 2d). The free energy profiles were calculated by free energy perturbation (FEP) method of Zwanzig[47] applied to the vertical motion of an explicit tip model (a 72 ion CaF_2 cluster) sampled using molecular dynamics simulation. $F(\boldsymbol{r})$ profiles were determined by numerical differentiation of the free energy profiles with respect to z (only the component of the force perpendicular to the interface affects the oscillation frequency of the cantilever in the mode of operation used here).

Simulations were carried out using classical molecular dynamics as implemented in the version 4 series of the GROMACS code.[48] The force-field describing CaF_2 and water-CaF_2 interactions was taken from de Leeuw,[49] discarding polarization terms. To describe water the TIP4P/2005 model was used.[50] We applied a 0.9 nm cut-off to treat non-bonded interactions and smooth particle mesh Ewald method to treat electrostatics.[51] The equations of motion were integrated using a 2 fs time step, and the LINCS algorithm was used to enforce rigid water geometries. An NPT ensemble (300 K, 1 atm) was generated using Berendsen thermostats and barostats, with time constants of 1.0 and 10.0 ps for temperature and pressure, respectively. The first 0.5 ns of the 4 ns simulations were discarded as equilibration periods.

Acknowledgement

Supporting Information Available

The supporting information includes three figures. These materials explain how we processed the experimental and simulated data to prepare the 3D $F_{\mathrm{exp}}(\boldsymbol{r})$ and $\rho(\boldsymbol{r})$ images. Figure

S1: the average filtering process used for preparing the 3D $\Delta f(\boldsymbol{r})$ image. Figure S2: the subtraction of LR force component from the 3D $F_{\mathrm{exp}}(\boldsymbol{r})$ image. Figure S3: the average filtering process used for preparing the 3D $\rho(\boldsymbol{r})$ image.

This material is available free of charge via the Internet at `http://pubs.acs.org/`.

References

(1) Raiteri, P.; Gale, J. D.

(2) Dong, G.; Teo, P.; Wickens, Z. K.; Grubbs, R. H. *Science* **2011**, *333*, 1609.

(3) Ostmeyer, J.; Chakrapani, S.; Pan, A. C.; Perozo, E.; Roux, B. *Nature* **2013**, *501*, 121.

(4) Krepkiy, D.; Mihailescu, M.; Freites, J. A.; Schow, E. V.; Worcester, D. L.; Gawrisch, K.; Tobias, D. J.; White, S. H.; Swartz, K. J. *Nature* **2009**, *462*, 473.

(5) Cheung, M. S.; García, A. E.; Onuchic, J. N. *Proc. Natl. Acad. Sci.* **2002**, *99*, 685.

(6) Bae, S.; Taylor, R.; Hernández-Cruz, D.; Yoon, S.; Kilcoyne, D.; Monteiro, P. J. M. *J. Am. Chem. Soc.* **2015**, *98*, 2914.

(7) Vorobiev, A.; Dennison, A.; Chernyshov, D.; Skrypnychuk, V.; Barbero, D.; Talyzin, A. V. *Nanoscale* **2014**, *6*, 12151.

(8) Donaldson, S. H.; Das, S.; Gebbie, M. A.; Rapp, M.; Jones, L. C.; Roiter, Y.; Koenig, P. H.; Gizaw, Y.; Israelachvili, J. N. *ACS Nano* **2013**, *7*, 10094.

(9) Fukuma, T.; Higgins, M. J.; Jarvis, S. P. *Biophys. J.* **2007**, *92*, 3603.

(10) Fukuma, T. *Sci. Technol. Adv. Mater.* **2010**, *11*, 033003.

(11) Kobayashi, K.; Oyabu, N.; Kimura, K.; Ido, S.; Suzuki, K.; Imai, T.; Tagami, K.; Tsukada, M.; Yamada, H. *J. Chem. Phys.* **2013**, *138*, 184704.

(12) Imada, H.; Kimura, K.; Onishi, H. *Langmuir* **2013**, *29*, 10744.

(13) Foster, A. S.; Barth, C.; Shluger, A. L.; Reichling, M. *Phys. Rev. Lett.* **2001**, *86*, 2373.

(14) Harada, M.; Tsukada, M. *Phys. Rev. B* **2010**, *82*, 035414.

(15) Watkins, M.; Shluger, A. L. *Phys. Rev. Lett.* **2010**, *105*, 196101.

(16) Watkins, M.; Berkowitz, M. L.; Shluger, A. L. *Physical Chemistry Chemical Physics* **2011**, *13*, 12584–12594.

(17) Fukuma, T.; Reischl, B.; Kobayashi, N.; Spijker, P.; Canova, F. F.; Miyazawa, K.; Foster, A. S. *Phys. Rev. B* **2015**, *92*, 155412.

(18) Watkins, M.; Reischl, B. *J. Chem. Phys.* **2013**, *138*, 154703.

(19) Amano, K.-I.; Suzuki, K.; Fukuma, T.; Takahashi, O.; Onishi, H. *J. Chem. Phys.* **2013**, *139*, 224710.

(20) Spijker, P.; Hiasa, T.; Musso, T.; Nishioka, R.; Onishi, H.; Foster, A. S. *J. Phys. Chem. C* **2014**, *118*, 2058.

(21) Senguttuvan, N.; Aoshima, M.; Sumiya, K.; Ishibashi, H. *J. Cryst. Growth* **2005**, *280*, 462–466.

(22) Nicoara, I.; Stef, M.; Pruna, A. *J. Cryst. Growth* **2008**, *310*, 1470–1475.

(23) Wakahara, S.; Furuya, Y.; Yanagida, T.; Yokota, Y.; Pejchal, J.; Sugiyama, M.; Kawaguchi, N.; Totsuka, D.; Yoshikawa, A. *Opt. Mater.* **2012**, *34*, 729–732.

(24) Zhang, Y.; Xiang, X.; Weber, W. J. *Nucl. Instr. and Meth.* **2008**, *266*, 2750–2753.

(25) Aoba, T.; Fejerskov, O. *Crit. Rev. Oral Biol. Med.* **2002**, *13*, 155–170.

(26) Prymak, O.; Sokolova, V.; Peitsch, T.; Epple, M. **2006**, *6*, 498–506.

(27) Hamza, S. M.; Hamdona, S. K. *J. Phys. Chem.* **1991**, *95*, 3149–3152.

(28) Amjad, Z. *Langmuir* **1993**, *9*, 597–600.

(29) de Vreugd, C. H.; ter Horst, J. H.; Durville, P. F. M.; Witkamp, G. J.; van Rosmalen, G. M. *Coll. Surf. A* **1999**, *154*, 259–271.

(30) Tai, C. Y. *J. Cryst. Growth* **1999**, *206*, 109–118.

(31) Tai, C. Y.; P. C, . C.; Tsao, T. M. *J. Cryst. Growth* **2006**, *290*, 576–584.

(32) Eksteen, J. J.; Pelser, M.; Onyango, M. S.; Lorenzen, L.; Aldrich, C.; Georgalli, G. A. *Hydrometallurgy* **2008**, *91*, 104–112.

(33) Jordan, G.; Rammensee, W. *Surf. Sci.* **1997**, *371*, 371–380.

(34) Kobayashi, N.; Itakura, S.; Asakawa, H.; Fukuma, T. *J. Phys. Chem. C* **2013**, *117*, 24388.

(35) Sader, J. E.; Jarvis, S. P. *Appl. Phys. Lett.* **2004**, *84*, 1801.

(36) Jarvis, S. P.; Uchihashi, T.; Ishida, T.; Tokumoto, H.; Nakayama, Y. *J. Phys. Chem. B* **2000**, *104*, 6091.

(37) Uchihashi, T.; Higgins, M.; Nakayama, Y.; Sader, J. E.; Jarvis, S. P. *Nanotechnology* **2005**, *16*, S49.

(38) Fukuma, T.; Kobayashi, K.; Matsushige, K.; Yamada, H. *Appl. Phys. Lett.* **2005**, *87*, 034101.

(39) Kilpatrick, J.; Loh, S.-H.; Jarvis, S. P. *J. Am. Chem. Soc.* **2013**, *135*, 2628.

(40) Fukuma, T.; Onishi, K.; Kobayashi, N.; Matsuki, A.; Asakawa, H. *Nanotechnology* **2012**, *23*, 135706.

(41) Fukuma, T.; Kimura, M.; Kobayashi, K.; Matsushige, K.; Yamada, H. *Rev. Sci. Instrum.* **2005**, *76*, 053704.

(42) Fukuma, T.; Jarvis, S. P. *Rev. Sci. Instrum.* **2006**, *77*, 043701.

(43) Fukuma, T. *Rev. Sci. Instrum.* **2009**, *80*, 023707.

(44) Miyazawa, K.; Izumi, H.; Watanabe-Nakayama, T.; Asakawa, H.; Fukuma, T. *Nan-otechnology* **2015**, *26*, 105707.

(45) Akrami, S. M. R.; Nakayachi, H.; Watanabe-Nakayama, T.; Asakawa, H.; Fukuma, T. *Nanotechnology* **2014**, *25*, 455701.

(46) Reischl, B.; Watkins, M.; S.Foster, A. *J. Chem. Theory Comput.* **2012**, *9*, 600.

(47) Zwanzig, R. W. *J. Chem. Phys.* **1954**, *22*, 1420–1426.

(48) Hess, B.; Kutzner, C.; van der Spoel, D.; Lindahl, E. *J. Chem. Theory Comput.* **2008**, *4*, 435–447.

(49) de Leeuw, N. H.; Cooper, T. G. *J. Mater. Chem.* **2002**, *13*, 93–101.

(50) Vega, C.; Abascal, J. L. F.; Sanz, E.; MacDowell, L. G.; McBride, C. *J. Phys.: Condens. Matter* **2005**, *17*, S3283–S3288.

(51) Essmann, U.; Perera, L.; Berkowitz, M. L.; Darden, T.; Lee, H.; Pedersen, L. G. *J. Chem. Phys.* **1995**, *103*, 8577.

Graphical TOC Entry